PAUL SCHERRER INSTITUT
PSI

Memorandum

Datum: 19th March 2003

Von: Andreas Suter
Telefon: 42 38
Raum: WLGA / B23
e-mail: andreas.suter@psi.ch

An:

cc:

Analysis of the nonlocal effects in Pb and Nb

Contents

1 Overview

In the following sections I am going to describe the analysis performed on thin niobium– and lead–films. This films were measured during the `run XIII - 2001` and `run XIV - 2002`. The motivation for these experiments is the search for nonlocal effects (see Sec.6).

The discussion will be organized as follows: (i) In Secs.2–5 different methods to analyze the data will be presented[1]. They are rather general and hence not only valid for the case of superconductors. (ii) Sec.6 will give a brief overview about the theory needed for the quantitative analysis of the data. (iii) In Secs.7, 8 a detailed analysis will be presented. (iv) In order to crosscheck the results the same analysis methods were applied to $YBa_2Cu_3O_{7-\delta}$ which is a strong type II superconductor, i.e. $\lambda_L(0) \gg \xi(0)$, in which nonlocal effects should not play any significant rôle[2].

2 Mean Value Reconstruction

During the beam time we used the following scheme to analyze the data online:

- The reduced asymmetry $a(t)$ was fitted with $a(t) = a_0 \exp[-(\sigma t)^2/2] \cos(\omega t + \phi)$. The mean field value was taken, *i.e.* $\langle B \rangle \propto \omega$.
- From `trim.sp` the mean stopping distance $\langle z \rangle$ for a given energy was taken.
- $B(z)$ was approximated by $\langle B \rangle$ vs. $\langle z \rangle$.

The question is if this scheme is any good. A very crude mathematical treatment shows that a footing along this line might be not too bad, though it doesn't describe exactly the procedure described above. The difference between the mathematical treatment and the online analysis is that in the model the "real" $\langle B \rangle$ is calculated, whereas in the online analysis a Gaussian $\langle B \rangle_G$ is estimated. Two models can be calculated readily. Both relay on the fundamental equation linking real space (z) with field space (B),

$$p(B)dB = n(z)dz, \tag{1}$$

where $p(B)$ gives the probability to find a muon in in the interval $[B, B + dB]$, likewise $n(z)$ gives the probability to find a muon in in the interval $[z, z + dz]$. Both probability distributions need to be normalized.
First exponential B vs. z dependence is treated and afterwards a heavily damped oscillation[3]:

(i) Exponential $B(z)$: One has to find an approximate stopping distribution for the muons. A simple formula which mimics the essential features is

$$n(z) = n_0 \, (z_0 - z) \, z^4, \quad z \in [0, z_0], \tag{2}$$

where $n_0 = 30 \, z_0^{-6}$ is the normalization factor and z_0 the maximum distance which an implanted muon can reach (see also Fig.1).

[1] Yet another approach is given in Ref.[1]
[2] at least not in the observed temperature range. There are some speculations that in a d-wave superconductor there might be as well nonlocal effects at very low temperature $T \lesssim 1$K
[3] which is the result of the "extrem anomalous limit" of the BCS and Pippard theory (see Sec.6)

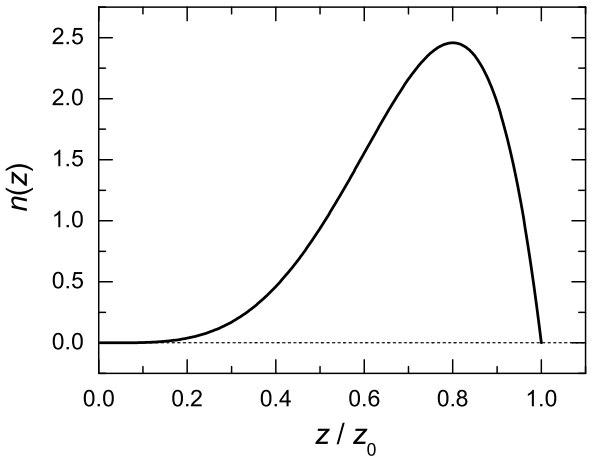

Figure 1: Toy stopping distribution of the muons.

The mean value of z is

$$\langle z \rangle = \frac{5}{7} z_0.$$

Assuming further

$$B(z) = B_{\text{ext}} \exp(-z/\lambda) \tag{3}$$

one gets

$$\begin{aligned} \langle B \rangle &= \int_0^{z_0} dz\, B(z) n(z) \\ &= B_0\, n_0 \lambda^2 \left[24\lambda^3 (z_0 - 5\lambda) + e^{-z_0/\lambda} \left\{ z_0^4 + 8\lambda z_0^3 + 36\lambda^2 z_0^2 + 96\lambda^3 z_0 + 120\lambda^4 \right\} \right] \\ &= B_0 \exp(-\langle z \rangle/\lambda) + f(\langle z \rangle), \qquad f(\langle z \rangle) > 0 \end{aligned}$$

with $\lim_{\langle z \rangle \to 0} f(\langle z \rangle) = 0$ and $f(\langle z \rangle) < \langle B \rangle(\langle z \rangle)$ in the first two decades which is shown in Fig.2. Notice that the curvature of $f(\langle z \rangle)$ is positive.

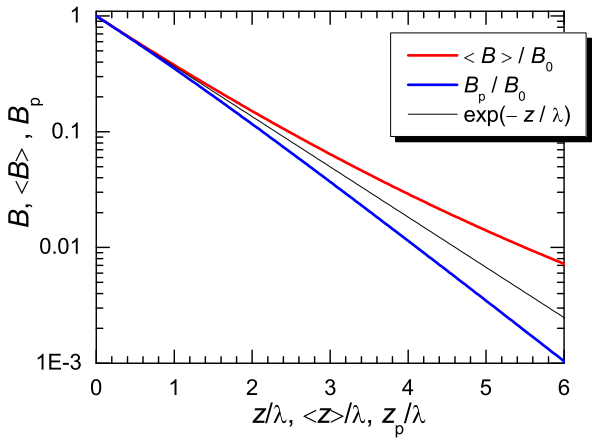

Figure 2: Functional dependence of $\langle B \rangle$ vs. $\langle z \rangle$ and $B_p(z_p)$ (see next section).

(ii) "Extreme Anomalous Limit" $B(z)$**:** The origin of this name will be clarified in Sec.6. The spatial dependence of the field is given as

$$B(z) \simeq B_0 \, \exp\left(-\frac{\sqrt{3}}{2}\,Qz\right) \, \cos\left(\frac{1}{2}\,Qz\right) \tag{4}$$

Since the result for $\langle z\rangle$ is already given, only $\langle B\rangle$ has to be calculated which is

$$\langle B\rangle/B_0 = c_0 + c_1 \exp\left(-\frac{7\sqrt{3}}{10}\,Q\langle z\rangle\right) \cos\left(\frac{7}{10}\,Q\langle z\rangle\right) + c_2 \exp\left(-\frac{7\sqrt{3}}{10}\,Q\langle z\rangle\right) \sin\left(\frac{7}{10}\,Q\langle z\rangle\right)$$

with the c_i's

$$\begin{aligned}
c_0 &= -\frac{1125000\,(7\sqrt{3}\,Q\langle z\rangle - 50)}{117649\,(Q\langle z\rangle)^6} \\
c_1 &= -\frac{375\,\left[150000 + 84000\,\sqrt{3}\,Q\langle z\rangle + 44100\,(Q\langle z\rangle)^2 - 2401\,(Q\langle z\rangle)^4\right]}{117649\,(Q\langle z\rangle)^6} \\
c_2 &= -\frac{375\,\left[12000 + 6300\sqrt{3}\,Q\langle z\rangle + 3920\,(Q\langle z\rangle)^2 + 343\sqrt{3}(Q\langle z\rangle)^3\right]}{16807\,(Q\langle z\rangle)^5}.
\end{aligned}$$

This formulaë look rather ugly but as can be seen in Fig.3, the result is very similar to the easier case discussed before.

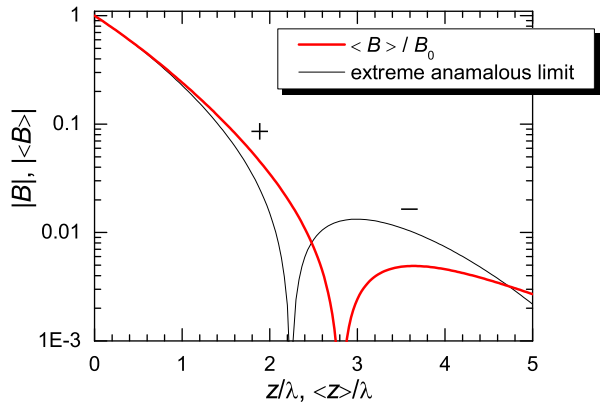

Figure 3: Functional dependence of $\langle B\rangle$ vs. $\langle z\rangle$ for the "extreme anomalous limit".

3 Peak Value Reconstruction

Analogous to the previous section one can study the functional dependence of B_p vs. z_p, where the subscript refer to the peak position of the corresponding distribution. Taking the same stopping distribution $n(z)$ (see Eq.(2)) one arrives at the following results.

(i) Exponential $B(z)$ **(Eq.3):** The z peak position is

$$z_p = \frac{4}{5}\,z_0.$$

To get the B_p one has to work a little harder. Eq.(1) gives the route, according to which

$$\begin{aligned}
p(B) &= n(z)\left|\frac{dB}{dz}\right|^{-1} \\
&= \frac{\lambda}{B}\,(\lambda\,\ln(B_0/B))^4\,(z_0 - \lambda\,\ln(B_0/B))\,, \qquad B \in [B_0 e^{-z_0/\lambda}, B_0]
\end{aligned}$$

Since we are only interested at the peak position, the normalization factor was suppressed. This is the formula which one allows to get B_p which is

$$\begin{aligned} B_p &= B_0 \exp\left[\frac{-1}{2\lambda}\left(z_0 - 5\lambda + \sqrt{(z_0+5\lambda)^2 - 4z_0}\right)\right] \\ &= B_0 \exp(-z_p/\lambda) - g(z_p), \quad g(z_p) > 0, \quad \lim_{z_p \to 0} g(z_p) = 0 \end{aligned}$$

This result is similar to the one in the last section, except that the curvature of $g(z_p)$ is *negative*.

(ii) "Extreme Anomalous Limit" $B(z)$**:** The peak position can not be calculated analytically.

4 Peak Value Reconstruction assuming Gaussian p(B)

The last case which can be calculated analytically and is perhaps closest to the online-analysis is that we assume a Gaussian field distribution

$$p(B) = \frac{1}{\sqrt{2\pi}\delta B} \exp\left[-\frac{1}{2}\left(\frac{B - B_0}{\delta B}\right)^2\right]. \tag{5}$$

According to Eq.(1), $n(z)$ can be calculated if an exponential $B(z)$ (Eq.(3)) is assumed, it takes the form

$$n(z) = \frac{1}{\sqrt{2\pi}\lambda} \frac{B_0}{\delta B} \exp\left[-\frac{1}{2}\left(\frac{B_{\text{ext}} e^{-z/\lambda} - B_0}{\delta B}\right)^2 - \frac{z}{\lambda}\right] \tag{6}$$

The peak values are than given by

$$\begin{aligned} B_p &= B_0 \\ n_p &= \lambda \ln\left[\frac{B_{\text{ext}}}{2\delta B^2}\left(\sqrt{B_0^2 + 4\delta B} - B_0\right)\right], \end{aligned}$$

which leads to

$$B_p(z_p) = B_{\text{ext}}\, e^{-z/\lambda}\left[1 - \left(\frac{\delta B}{B_{\text{ext}}}\right)^2 e^{+2z_p/\lambda}\right]. \tag{7}$$

This results are collected in Fig.4. As one can see, it shows the same trend as the peak value reconstruction described in Sec.3. The $n(z)$ profile seems the be a little less realistic compared to the one used above.

5 Integral Reconstruction

In case the statistics of the data is not too bad it is possible to reconstructed the B vs. z relation directly from Eq.(1). Integrating both sides of Eq.(1) leads to

$$\int_0^z n(\zeta)\, d\zeta = 1 - \int_z^\infty n(\zeta)\, d\zeta = \int_B^\infty p(\beta)\, d\beta = 1 - \int_0^B p(\beta)\, d\beta,$$

which is, for a given z, an equation for B. However, this is only true if $p(B), n(z)$ are monotonic functions. Figure 5 visualizes this very idea.
Mathematically starting the z-Integration at $z = 0$ (red shaded area in Fig. 5) is equivalent as to start the z-Integration deep inside the sample (blue shaded area in Fig. 5). However, with real experimental data this is not always true. There are two main reasons:

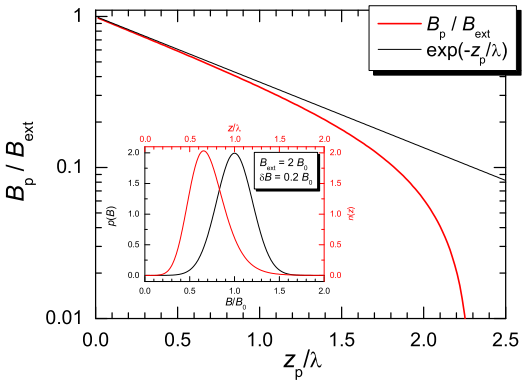

Figure 4: B_p vs. z_p reconstruction for a Gaussian $p(B)$ and an exponential $B(z)$.

1. A background at the external field B_{ext} is very often present in the real data. A correction by hand of this background may lead to a slightly wrong $p(B)$.

2. `MaxEnt` has a hard time to cope with small B-fields[4]. The reason is the exponential decay of the Muon (life time), leading to a final line width of the signal which first has to be taken care off. From this point of view, it is better starting the z-integration at the very surface of the sample.

In practise one has to decide for every single run what makes more sense, however, very often the second point proofed to be the more sever handicap. Furthermore one finds very often some artefacts at the very beginning of $B(z)$ and the very tail in the reconstruction. Some are very well understood and are going to be described in the following. (i) Kink upturn for $z \to 0$: This is due to the uncertainty in the external background. The feature (if there) is always very pronounced and hence it is very clear where to cut. (ii) Downturn for $z \to z_{\max}$, where $z_{\max}$ is the maximal implantation distance for the muon: I am not quite sure yet. I think the reason is that $n(z)_{\text{trim.sp}}$ for $z \to z_{\max}$ does not show a perfect correspondence with the real $n(z)$ anymore. Another effect enters through the difference in the binning of the data. This also can lead to a downturn as on finds from crosschecks with artificial data. This feature is always there and it less clear where to cut. I always cut off rather more to be on the save side.

6 Theory

One is used to think in the London approximation in which "perfect diamagnetism" leads to the very simple relation between the current density $\boldsymbol{j}_{\text{D}}$ and the vector potential $\boldsymbol{A}$ [2, 3, 4]

$$\boldsymbol{j}_{\text{D}} = -\frac{1}{\mu_0} \underbrace{\mu_0 \frac{ne^2}{m}}_{=:\,\lambda_{\text{L}}^{-2}} \boldsymbol{A} \tag{8}$$

with μ_0 the magnetic permeability of free space, e the electronic charge, m the electronic mass, and n is the superfluid density[5]. This results, for a semiinfinite surface, in an exponential decaying magnetic field

$$h(z) = h_{\text{ext}} \exp(-z/\lambda_{\text{L}})$$

Since the Meissner–Ochsenfeld effect is not only "perfect diamagnetism" this picture is somewhat too crude. A very simple picture might also help to realize that something is missing.

[4] small means smaller than the life time of the muon, or more precise $B \lessapprox 1/(\gamma\tau) = 5.34$ G

[5] In a phenomenological twofluid model, e is the electrical charge of the charge carriers, i.e. $2e$ for a Cooper pair, and m the mass of these charge carriers, i.e. $2m$ for a Cooper pair.

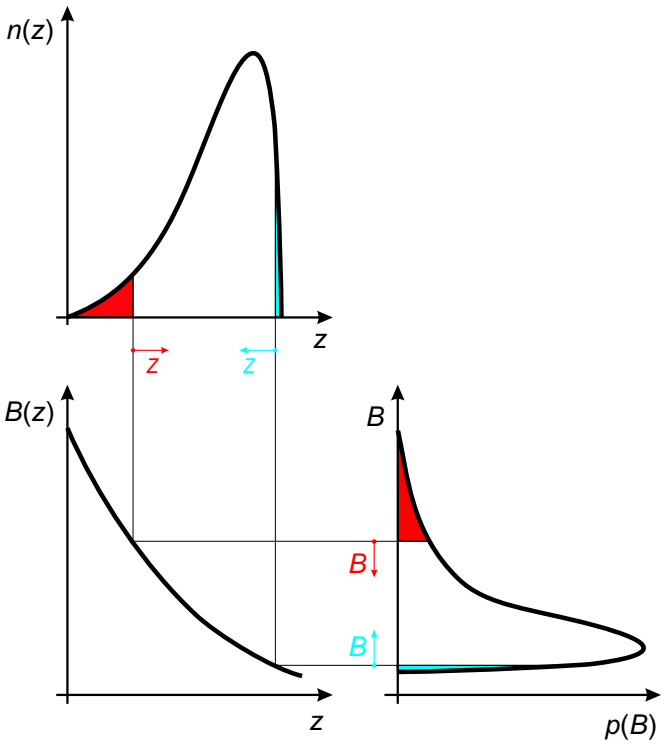

Figure 5: Sketch of the relation between $n(z)$, $B(z)$, $p(B)$. The colored areas show the reconstruction pathes.

Fig.6 shows two situations: (i) $\lambda \gg \xi$ here the magnetic field is approximately constant over the characteristic length ξ of the superfluid charge carriers which are responsible for the Meissner–Ochsenfeld screening. In this situation the local description is sufficient. (ii) $\lambda \ll \xi$ in this situation there is a drastic change of the magnetic field over the distance ξ and hence the local description must break down. The real Meissner–Ochsenfeld screening current consists of two parts, a diamagnetic one as above and a paramagnetic one. In the real superconductor Eq.(8) goes over into[6]

$$j_\alpha(\boldsymbol{r}) = -\sum_\beta \int K_{\alpha\beta}(\boldsymbol{r}-\boldsymbol{r}')A_\beta(\boldsymbol{r}')d\boldsymbol{r}' \tag{9}$$

which after Fourier transformation in respect to $\boldsymbol{r}$ is

$$j_\alpha(q) = -\sum_\beta K_{\alpha\beta}(q)A_\beta(q). \tag{10}$$

The magnetic field penetrating a semiinfinite surface of a superconductor in the Meissner–Ochsenfeld state is then given as (assuming $K_{\alpha\beta}$ to be isotropic)

$$h(z) = h_0 \,\mathrm{Im}\left\{\mathcal{F}_q\left[\frac{q}{q^2+K(q,T)}\right]\right\} \tag{11}$$

where $\mathcal{F}_q[\ldots]$ means Fourier transform in respect to q. This reduces obviously to an exponential decay if $K(q,T)$ is a constant. Strictly speaking, Eq.(11) is only valid in the case of specular reflection at the surface. There is another analytical formula available if one assumes only diffuse scattering at the surface. A quantitative analysis shows [4] that the difference is only marginal and since the real system wont by in neither off these two limits, I will stick to Eq.(11).

[6] only linear response is considered! Further a translational invariant system is assumed.

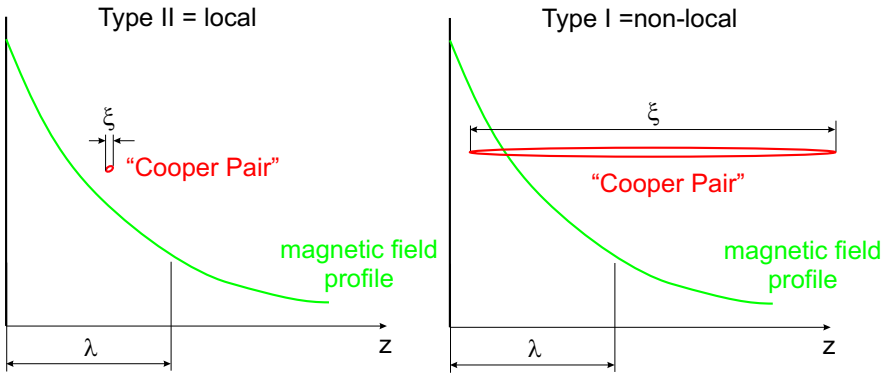

Figure 6: The left panel shows a typical type II situation. Here the change of the magnetic field over the size of a Cooper pair ξ is negligible and hence a local $\boldsymbol{j}$-$\boldsymbol{A}$ is sufficient. The right panel shows the situation of a type I superconductor. Here the magnetic field changes dramatically over the distance of ξ and hence the local approximation must break down.

6.1 Pippard

Pippard [5] was the first to realize that under some circumstances the London approximation breaks down, nota bene before the BCS theory was borne. He found experimentally as well as theoretically that an additional intrinsic length scale has to exist, which is the coherence length ξ_{P}. He found a kernel which is actually very close to the BCS one

$$\mu_0 K_{\mathrm{P}}(q,T) = \frac{1}{\lambda_{\mathrm{L}}^2(T)} \frac{\xi_{\mathrm{P}}(T)}{\xi_{\mathrm{P}}(0)} \left[\frac{3}{2} \frac{1}{(q\xi_{\mathrm{P}}(T))^3} \left\{ \left(1 + (q\xi_{\mathrm{P}}(T))^2\right) \arctan(q\xi_{\mathrm{P}}(T)) - q\xi_{\mathrm{P}}(T) \right\} \right]. \quad (12)$$

The q–dependence of the kernel is shown in Fig.7. The real-space $\boldsymbol{j}$–$\boldsymbol{A}$ relation in the Pippard approximation is then given by

$$\boldsymbol{j}(\boldsymbol{r}) = -\frac{1}{\mu_0} \frac{3}{4\pi} \frac{1}{\lambda_{\mathrm{L}}^2(T)\,\xi_{\mathrm{P}}(T)} \int \frac{\boldsymbol{R}[\boldsymbol{R}\cdot\boldsymbol{A}(\boldsymbol{r}')]\, e^{-R/\xi_{\mathrm{P}}(T)}}{R^4}\, d\boldsymbol{r}', \quad (13)$$

with $\boldsymbol{R} = \boldsymbol{r} - \boldsymbol{r}'$.
The *weak* temperature dependence of $\xi_{\mathrm{P}}(T)$ was only explained by the BCS theory. This can be written as

$$\frac{1}{\xi_{\mathrm{P}}(T)} = \frac{J(0,T)}{\xi_{\mathrm{P}}(0)} + \frac{1}{\ell} \quad (14)$$

where ℓ is the electronic mean free path and

$$J(0,T) = \left(\frac{\lambda(T)}{\lambda(0)}\right)^2 \frac{\Delta(T)}{\Delta(0)} \tanh\left[\frac{\Delta(T)}{2k_{\mathrm{B}}T}\right]$$

The temperature dependence of $\xi_{\mathrm{P}}(T)$ for $\ell \to \infty$ is shown in Fig.8.

6.2 BCS

The BCS treatment leads to a very similar equation as Eq.(13) where only the exponential function has to be replaced by a more complicated one. Without giving here any details (see [2, 6]) this leads to the kernel

$$\mu_0 K_{\mathrm{BCS}}(q,T) = \sum_{n=0}^{\infty} \frac{1}{\Lambda_n(T,\ell)} \cdot g(q\xi_n(T,\ell)) \quad (15)$$

with the following set of abbreviations

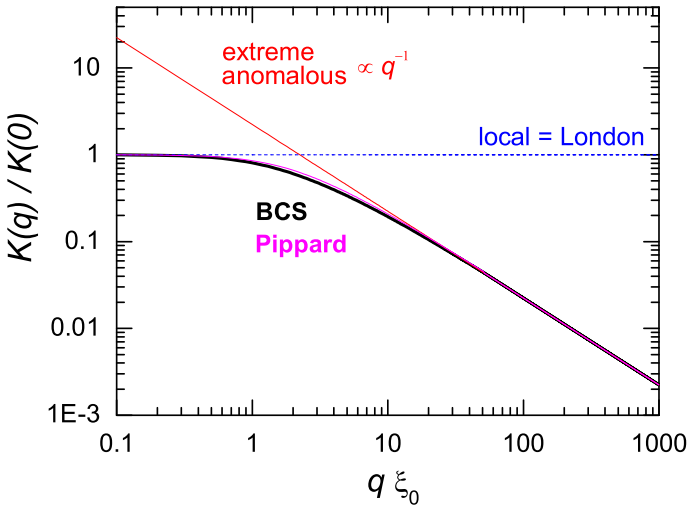

Figure 7: q–dependence of the different kernels. The blue dashed line represents the London approximation. Since it is a constant in q, obviously a delta function results in z, i.e. a local relation. The BCS- (black) and Pippard-kernel (magenta) are very similar and have a q^{-1} asymptotic behavior for $q \to \infty$.

$$
\begin{aligned}
\Lambda_n(T,\ell) &= \frac{1}{2a}\,\lambda_{\mathrm{L}}^2 f_n^3 \left(1+\frac{\xi_n(T,\ell)}{\ell}\right) \\
g(x) &= \frac{3}{2}\frac{1}{x^3}\left\{\left(1+x^2\right)\arctan(x)-x\right\}, \qquad \lim_{x\to 0} g(x) = 1 \\
\\
\xi_n(T,\infty) &= \frac{\pi}{2}\,\frac{\xi_0}{f_n}\,\frac{\Delta(0)}{\Delta(T)}, \qquad \frac{1}{\xi_n(T,\ell)} = \frac{1}{\xi_n(T,\infty)} + \frac{1}{\ell} \\
a &= \pi\,\frac{k_{\mathrm{B}}T}{\Delta(T)} = \gamma\,\frac{t}{\delta(t)} = 1.7811\,\frac{t}{\delta(t)}, \quad t=\frac{T}{T_c},\ \delta(t)=\frac{\Delta(T)}{\Delta(0)} \\
f_n &= \sqrt{1+(2n+1)^2a^2} \\
\xi_0 &= \frac{\hbar v_{\mathrm{F}}}{\pi\Delta(0)}, \quad \Delta(0) = \frac{\pi}{\gamma}\,k_{\mathrm{B}}T_c = 1.764\,k_{\mathrm{B}}T_c
\end{aligned}
$$

with $\gamma = 1.7811\ldots$ the Euler constant. Though this expressions looks much more complicated compared to the Pippard relation, there are only slight deviation as long as $T \lesssim 0.9T_c$.
The temperature dependence of $\lambda_{\mathrm{L}}(T)$, within the BCS theory, is defined by the following equation ($\ell \to \infty$)

$$
\mu_0 K_{\mathrm{BCS}}(q=0,T,\ell\to\infty) = \frac{1}{\lambda_L^2(T)} = \sum_{n=0}^{\infty}\frac{1}{\Lambda_n(T,\infty)} = \frac{1}{\lambda_L^2(0)}\sum_{n=0}^{\infty}\frac{2a}{(1+(2n+1)^2a^2)^{3/2}} \tag{16}
$$

6.3 $h(z)$ for a semiinfinite sample surface

After have written down all these formulaë the question is: How does the field dependence alter by all this? As shown at the beginning of this section the field decays exponentially in the local limit. Within the BCS and Pippard theory there is no analytical formula available and the $h(z)$ dependence has to be calculated numerically according to Eq.(11). There is one other interesting limit which can be treated analytical which is the extreme anomalous limit. In this limit the real kernel is replaced by its $q \to \infty$ asymptotic behavior which is

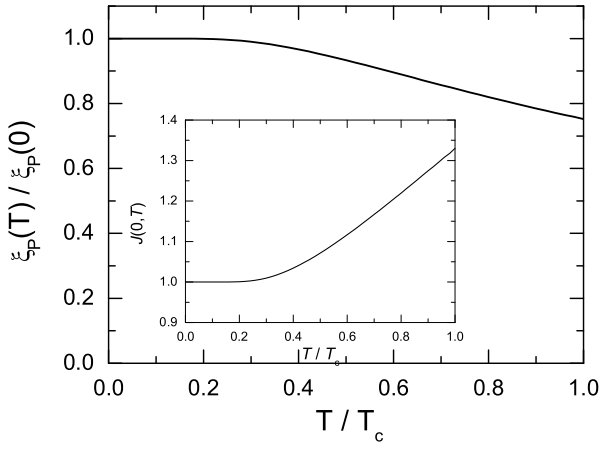

Figure 8: Temperature dependence of the "modified" Pippard coherence length $\xi_{\rm P}(T)$.

$$\mu_0 K_{\rm ea}(q) = \frac{3\pi}{4}\,\frac{1}{\lambda_{\rm L}^2\xi_0}\,q^{-1}$$

Carrying out the Fourier transform in Eq.(11) leads to[7]

$$h(z) \simeq h_{\rm ext}\,\exp\left(-\frac{\sqrt{3}}{2}\,Qz\right)\cos\left(\frac{1}{2}\,Qz\right), \qquad Q = \left[\frac{3\pi}{4}\,\frac{1}{\lambda_{\rm L}^2\xi_0}\right]^{1/3} \tag{17}$$

Fig.9 shows for two cases (Aluminum, Lead), how the different $h(z)$'s depend upon the models. The main effect off the non–locality of the kernels are two folded: (i) There is a sign reversal of the field at $z/\lambda_{\rm L} \gtrapprox 5$. The maximum amplitude of the reversed field is around two orders of magnitude smaller than the external field, making it rather hard to detect in our μSR experiments. (ii) $h(z)$ shows a clear negative curvature. This is a much more reliable feature than sign reversal of the field.

6.4 Strong coupling limit

Now, there is a problem with Niobium and Lead. Both are not very well described in the simple BCS model which assumes only a weak coupling between the electron and the phonons. Further no spin-orbit coupling is present in the weak coupling BCS model. The first point is *neither* for Niobium *nor* for Lead fulfilled. In the case of Lead also the second point is important.

Fortunately the general structure of the of the kernel $K(q,\omega\to 0)$ is the same as in Eq.(15) [7, 8, 9]. The only changes are a different gap $\Delta_{\rm sc}(T)$ and an additional renormalization factor Z. These leads to a renormalization of (see also Sec.6.2 and Sec.A)

$$\begin{aligned}\Lambda_n(\Delta_{\rm BCS}) &\rightarrow \Lambda_n(\Delta_{\rm sc})Z\\ \xi_n(\Delta_{\rm BCS}) &\rightarrow \xi_n(\Delta_{\rm sc})/Z\end{aligned}$$

since the gap is only mildly affected (e.g. $2\Delta_{\rm BCS}(0)/k_{\rm B}T_c = 3.52$ whereas $2\Delta_{\rm sc}^{\rm Pb}(0)/k_{\rm B}T_c = 4.3$ [8], though the temperature dependence of $\Delta(T)$ is altered as well), the dominant part stems

[7] The exact solution would be $h(z)/h_{\rm ext} = 1/(2\sqrt{3\pi})\cdot 1/(2\pi i)\int ds\{\alpha^{-s}\Gamma(1/2-s)\Gamma(s)\Gamma(1/6+s)\Gamma^2(1/2+s)\Gamma(5/6+s)/(\Gamma(2/3-s)\Gamma(1/3-s))\}$, with $\alpha = \pi^2 z^6/(2^{10}3^4\,\lambda_{\rm L}^4\xi_0^2)$. This is a horrible thing and only slightly different than the given expression.

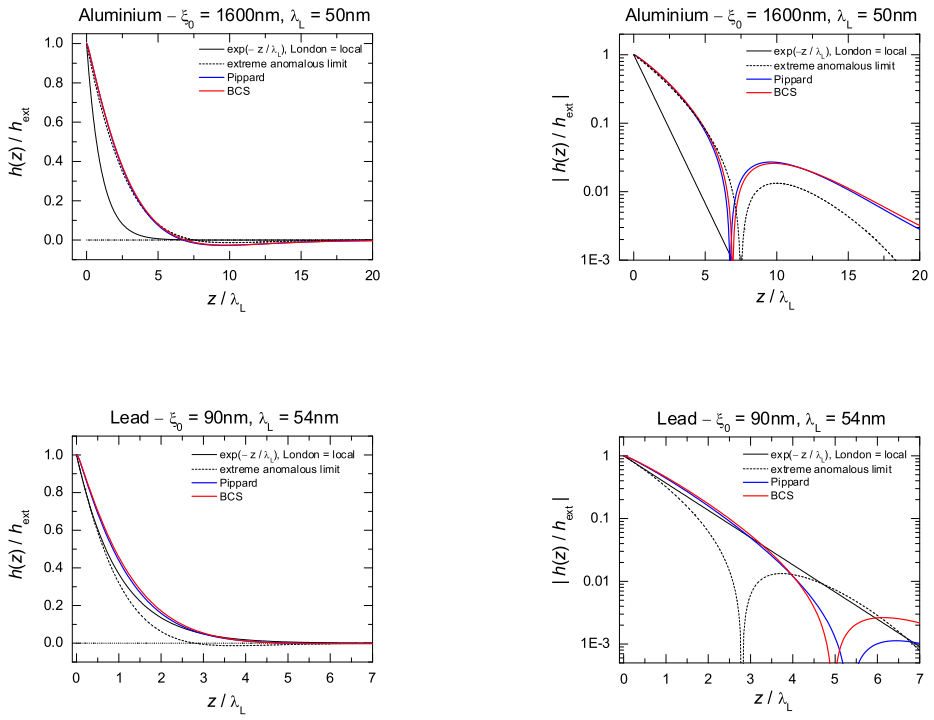

Figure 9: The top two figures show Aluminum, whereas the bottom two show Lead. As one can see, the differences between Pippard and BCS are small.

from the renormalization due to Z ($Z_{\mathrm{Pb}} \approx 2.5$). This change does not changing the *form* of the kernel, rather it is altering its amplitude, hence all the features describing $h(z)$ are still present albeit the field reversal is weekend even more.

6.5 Zoology of λ and ξ

Here a warning: λ is not λ! No, seriously, there are quite a few different definitions of λ and ξ as will be shown below. The first water shed is between the microscopic definitions of λ and ξ and the Ginzburg–Landau (GL) ones. Whereas in GL approach $1/\xi$ describes something like the stiffness of the order parameter with a very strong temperature dependence as approaching T_c, the ξ in BCS theory is rather something like the diameter of a Cooper-Pair and hence only very weakly temperature dependant.

For λ it is even worse. There are several different definitions within the microscopic approach, which I will try to list below. Lets start with the local theory where there actual all the different definition gives the same result.

Definition 1: Since $h(z) = h_{\mathrm{ext}} \exp(-z/\lambda)$ the field dependence itself defines a natural length scale λ.

Definition 2:

$$\lambda_{\mathrm{int}} := \frac{1}{h_{\mathrm{ext}}} \int_0^\infty dz\, h(z) \tag{18}$$

which results, of course, in the same λ if $h(z) \propto \exp(-z/\lambda)$.

Definition 3: Yet another definition is given by Eq.(16), i.e.

$$\mu_0 K_{\mathrm{BCS}}(q = 0, T, \ell \to \infty) =: \frac{1}{\lambda_L^2(0)} \cdot f(T)$$

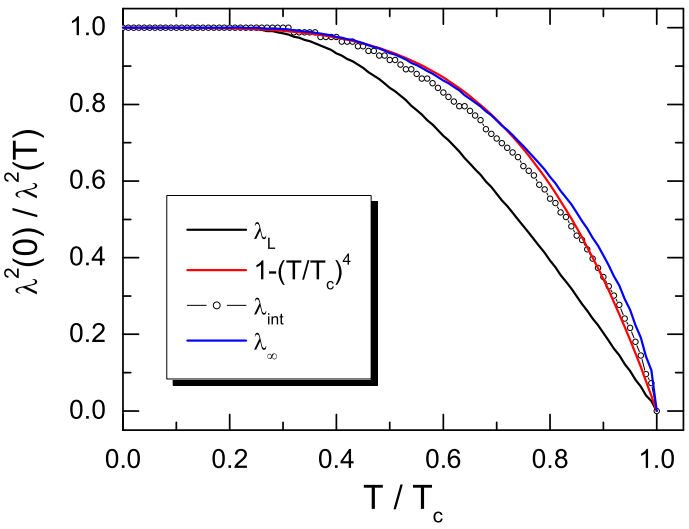

Figure 10: Temperature dependence of $(\lambda(0)/\lambda(T))^2$. Black: Temperature dependence according to Eq.(16). Red: The two fluid ansatz. Blue: The extreme anomalous limit (see Eq.(19)). Open symbols: The integral definition of λ based on Eq.(18) with parameters for Aluminum.

Now in the situation where $h(z)$ is deviating from the exponential function, these different definitions lead to different results! Therefore it is essential to define what one is referring to. E.g. in the case of the extreme anomalous limit (see Eq.(4)), definition 1 gives something like

$$\lambda_{\rm ea} = \frac{2}{\sqrt{3}}\,\frac{1}{Q} = \frac{2}{\sqrt{3}}\,\left(\frac{4}{3\pi}\right)^{1/3}\left(\lambda_{\rm L}^2\xi_0\right)^{1/3} \simeq 0.8678\,\left(\lambda_{\rm L}^2\xi_0\right)^{1/3},$$

definition 3 will lead to an undefined λ_∞ and the only reasonable definition 2 gives

$$\lambda_\infty = \frac{1}{h_{\rm ext}}\int_0^\infty dz\, h(z) = \left[\frac{3}{(2\pi)^2}\right]^{1/6}\left(\lambda_{\rm L}^2\xi_0\right)^{1/3} \simeq 0.6508\,\left(\lambda_{\rm L}^2\xi_0\right)^{1/3} \tag{19}$$

Interesting at this equation is that it shows that λ_∞ has a very different temperature dependence than $\lambda_{\rm L}$. That the temperature dependence are indeed rather different can be seen from Fig.10. For $\lambda_{\rm int}$ I chose parameters of Aluminum, if I rather would have used Lead the curve would "shift" in the direction of $\lambda_{\rm L}$. This shows that $\lambda(T)$ is *not* an universal curve, i.e. its details depend on the actual material parameters.

In my analysis I used Eq.(12) and Eq.(15) in the limit $q \to 0$ as a working definition of $\lambda_{\rm L}(0)$. Furthermore the full equations mentioned here were the basis to derive ξ_0. In the case of the Pippard model $\xi(T)$ as in Eq.(14) was used and a two fluid model temperature dependence of $\lambda_{\rm P} = \lambda_{\rm L}(0)/\sqrt{1-t^4}$ with $t = T/T_c$. The temperature dependence of the gap $\Delta(T)$ was taken from Ref. [10]. Since the temperature dependent strong coupling corrections are rather small [9] they were *not* included in the fitting itself.

7 Niobium

7.1 Characterization of the films, Experimental Details

Rustem measured resistance as well as the magnetization of the niobium film. The samples he measured were co–sputtered on the same substrate as the film we measured by LEμSR. The results are shown in Fig.11.

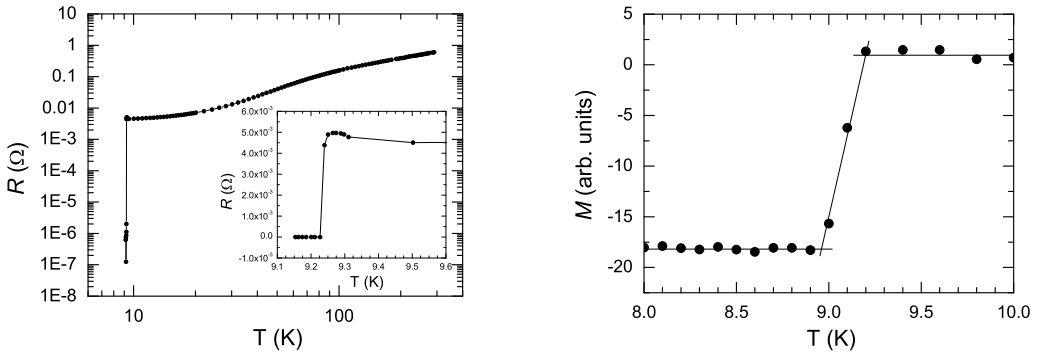

Figure 11: Left graph: Resistance of a part of the niobium film with a $T_c = 9.24(6)$ K. Right graph: Magnetization measurement showing the onset of the Meissner effect at $T_c = 9.2(1)$K.

The electron mean free path ℓ^{Nb} was estimated by Elvezio (see [11] and Appendix B) to be in the range of

$$\ell^{\mathrm{Nb}}(T = T_c) \approx 300 \ldots 500 \text{ nm},$$

i.e. our Nb sample is indeed in the extrem clean limit!

The oxide layer on top of the film an its thickness were determined by Rutherford backscattering (RBS). The thickness of the NbO layer is 4.2(0.3)nm whereas the niobium film itself has a thickness of 310(15)nm.

All the experiments were carried out in the "Mango cryostat". The temperature calibration for it was carried out by Rustem Khasanovs. This callibration was used and is shown in Fig.12.

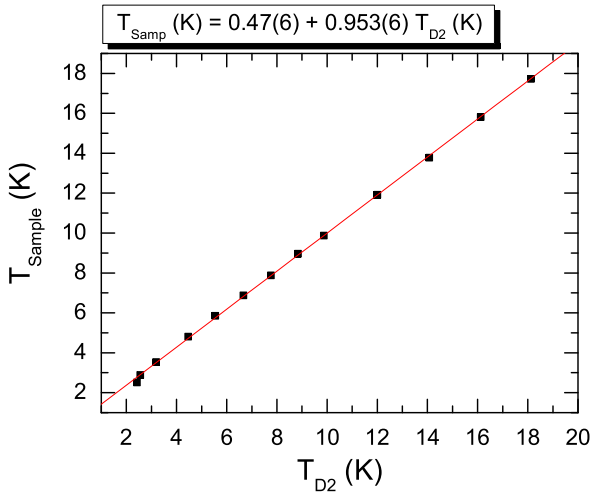

Figure 12: Temperature calibration for the "Mango cryostat".

7.2 Nb — Mean Value Reconstruction

As already mentioned in Sec.2 one method to reconstruct the penetration profile is the "Mean Value Reconstruction" which I will present here in some detail.

There are two things one has to know: (i) How does the stopping distribution $n(z)$ of the muons looks like, and what is a sensible measure to define a implantation energy E_{impl} versus distance relation? (ii) How do we analyze the μSR spectra to get a working definition of a

characteristic field? If we can answer these two questions this automatically will lead us to a way to reconstruct $B(z)$.

Lets consider the point (i): The stopping distribution of the muons is calculated by `trim.sp` [12]. That this monte-carlo code indeed gives a correct description of $n(z)$ was checked experimentally [13] and shows a rather nice correspondence. Some typical implantation profiles are shown in Fig.13. The simulated sample consist of a 5nm NbO layer followed by a very thick Nb one. The 5nm oxide layer was necessarily introduced since it changes especially the low energy implantation profiles. In the real sample the oxide layer thickness was determined by RBS as described in the previous section. A detailed analysis of the oxidation of niobium is given in Ref.[14]. Now coming back to the question what is a reasonable length scale to describe the E_{impl} versus z relation, there are two obvious possibilities, namely the peak value position z_{P} of $n(z)$ or the mean value position $\langle z \rangle$. As already discussed in Secs.2, 3 the mean value reconstruction is the more appropriate one in our case since the small systematic errors introduced *cannot* mimic nonlocal effects! Therefore only this method was considered in the following analysis.

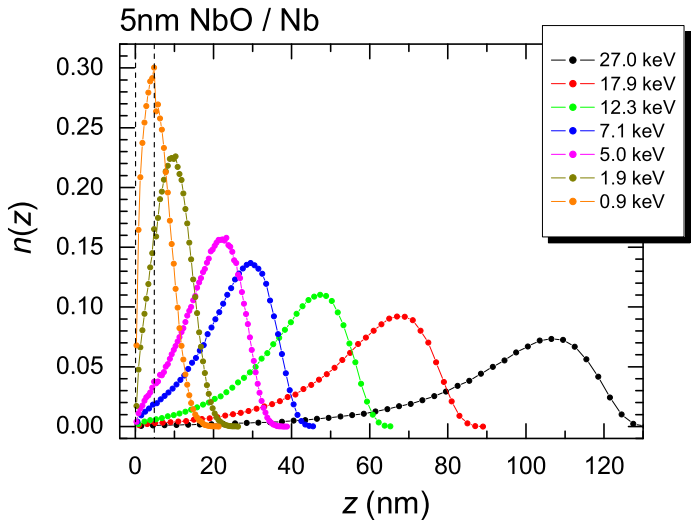

Figure 13: Myon stopping distribution in Niobium calculated by `trim.sp`. On top a 5nm NbO film was introduced in the calculation.

The top graph of Fig.14 shows E_{impl} vs. $\langle z \rangle$ for this film which reveals an almost perfect linear relationship.

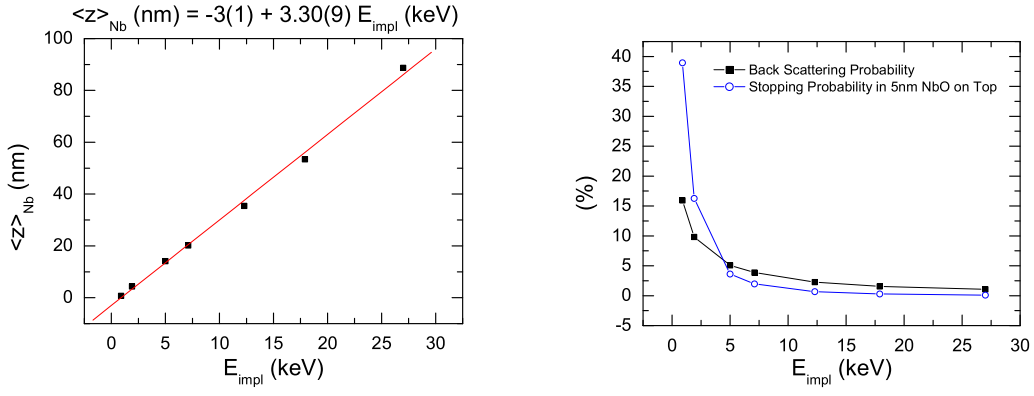

Figure 14: Left graph: E_{impl} vs. $\langle z \rangle$. Right graph: The closed black symbols show the backscattering probability of muons from the surface as function of E_{impl}. The blue open symbols show the stopping probability of the muons in the top layer of NbO.

Now I will come to point (ii), the estimate of the correct field. In Sec.2 the real $\langle B \rangle$ was calculated based on the knowledge of $B(z)$. This, however, is not available in the real experiment, since we do not know a priori the $B(z)$ functional dependence of our measured films, and hence another method is needed to get an estimate of $\langle B \rangle$. I proceeded as follows: The reduced asymmetry was fitted by the following expression

$$\begin{aligned} a(t) \quad = \quad & a_{\mathrm{BG}}^{\mathrm{tot}} \ \exp\left[-\frac{1}{2}\left(\sigma_{\mathrm{BG}} t\right)^2\right] \cos(\gamma_\mu B_{\mathrm{BG}} t + \phi) + \\ & a_{\mathrm{Nb}} \ \exp\left[-\frac{1}{2}\left(\sigma_{\mathrm{Nb}} t\right)^2\right] \cos(\gamma_\mu B_{\mathrm{Nb}} t + \phi) \end{aligned} \tag{20}$$

with $a_{\mathrm{Nb}} + a_{\mathrm{BG}}^{\mathrm{tot}} + a_{\mathrm{BS}} = 0.27$ which is the maximal achievable asymmetry in our LEμSR apparatus. All these terms are explained in Table 1. The different asymmetries as function of E_{impl} are shown in Fig.15. Two of these parameters are of special interest which is B_{Nb} which is used for the "mean value reconstruction" of $B(z)$ and the depolarization rate $\sigma_{\mathrm{Nb}}(E_{\mathrm{impl}})$ which I am going to discuss only in Sec.8. All the fits were carried out using `WKM`. The whole $B(z)$ reconstruction extracted in this way is shown and discussed together with the integral reconstruction in Sec.7.4.

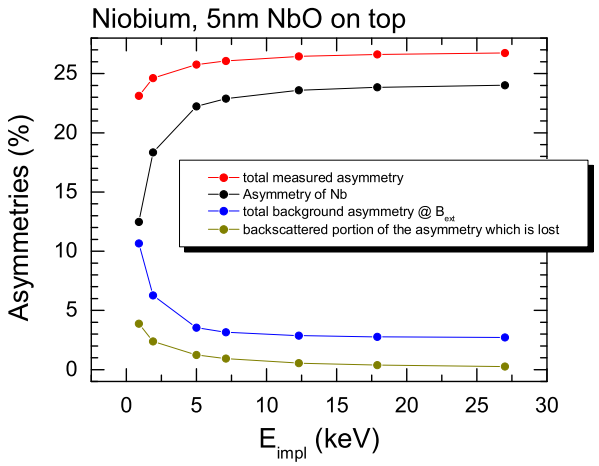

Figure 15: Different asymmetries as function of E_{impl}.

Parameter	Description	fit comment
α	asymmetry in detector efficiency	free
ϕ	relative phase between spin and first detector.	free
a_{BS}	portion of muons which is backscattered from the surface. Their asymmetry is assumed to be lost from the spectrum.	fixed according to `trim.sp`
$a_{\mathrm{BG}}^{\mathrm{tot}}$	$= a_{\mathrm{PbO}} + a_{\mathrm{BG}}$	fixed according to `trim.sp`
σ_{BG}	depolarization rate of the background	free
B_{BG}	background field assumed at the external field B_{ext}	fixed according to $T > T_c$ measurement
a_{Nb}	portion of the muons stopping in Nb.	fixed according to `trim.sp`
σ_{Nb}	depolarization rate of the Nb signal	free
B_{Nb}	approximation of $\langle B \rangle$. I.e. one assumes a Gaussian $p(B)$.	free
a_{PbO}	portion of the muons which stop in the PbO. It is assumed that they experience B_{ext}.	fixed according to `trim.sp`
a_{BG}	$\approx 10\%$ of the muons do not hit the sample and stop at a place where they experience B_{ext}.	$= 0.027$

Table 1: Description of the different terms contributing to the measured spectrum according to Eq.(20). The maximal achievable asymmetry in our setup is $a_{\mathrm{Nb}} + a_{\mathrm{BG}}^{\mathrm{tot}} + a_{\mathrm{BS}} = 0.27$.

7.3 Nb — Integral Reconstruction

As described in Sec.5 the integral reconstruction does have the advantage that in principle a single implantation energy can give the whole $B(z)$ curve and hence reducing the measuring time dramatically. Though, the analysis shows that one should have something like 10^6 counts in order not to suffer too much from poor statistics. This is not always fulfilled for the niobium data. The numerical algorithm used for the reconstruction are straight forward and were carried out in `matlab`. The source of the small routines used is given in the Appendix D.

7.4 Nb — Results and Discussion

The fitting of $B(z)$ was carried out for the Pippard formulaë Eqs.(11) & (12) and for the weak coupling BCS formulaë Eqs.(11) & (15)[8]. The fitting program (`non_local_sc.exe`) is written in C. The `minuit` fitting library from cern [15] was used, furthermore the FFT routine from the nag library [16] was taken, since it is much better than the one from the cern libs or the one from the "numerical recipes". For each single run exists a file `*_param.dat`, e.g. `nb_T2_6K_E071_1789_param.dat`, which shows the input parameters and the corresponding output parameters. Fig.16 shows the low temperature reconstruction for niobium. Table 2 summarizes all the fitting results.

T (K)	$h_{\mathrm{ext}}^{\mathrm{P}}$ (G)	λ_0^{P} (nm)	$h_{\mathrm{ext}}^{\mathrm{BCS}}$ (G)	λ_0^{BCS} (nm)
2.95(1)	97(3)	28(3)	96(3)	26(3)
7.60(1)	98(3)	31(3)	98(3)	26(3)

Table 2: Results of the Niobium analysis. A fixed value of $\xi_0 = 39$nm was used. Since the mean free path $\ell \gg \xi_0$, it was set to $\ell = 1000$nm.

[8] This is possible, since the strong coupling limit only leads to a renormalization as shown in Sec.6.4.

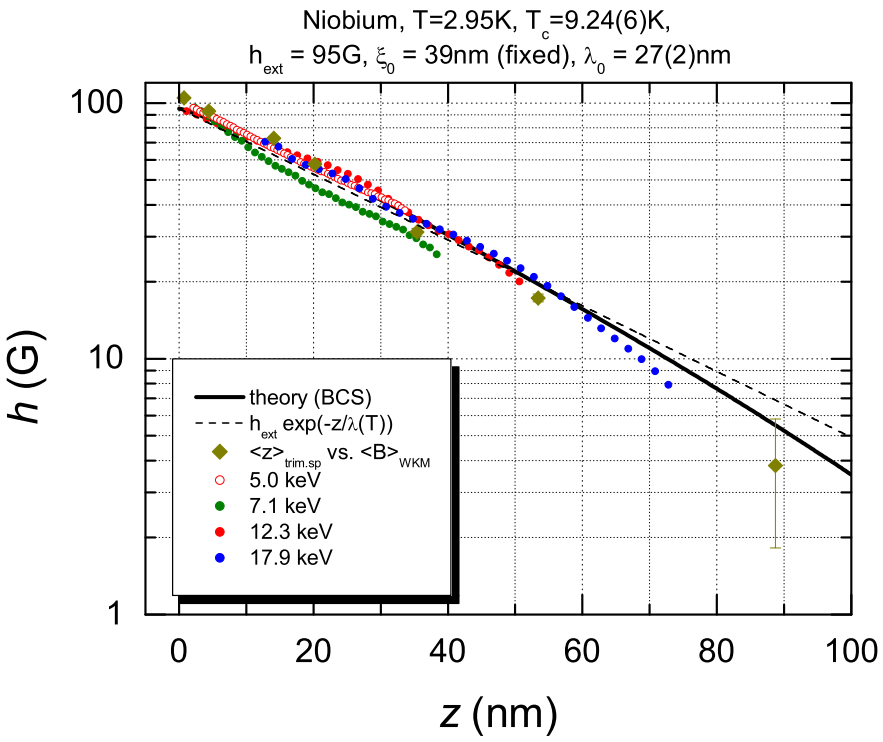

Figure 16: Niobium: B versus z reconstruction.

Here quite a few comments are needed, which I loosely will discuss now. Very crudely speaking the form of $B(z)$ can characterized in the following way: The slope of the curve is dominated by $\lambda(T)$ and therefore is a rather robust feature. The curvature, however, is given by the ratio $\lambda(T)/\xi_0 =: \varkappa$ and is only well defined if $\varkappa < 1$, which is true for lead, but not for niobium. Obviously it is going to get harder and harder to fit ξ_0 for $\varkappa \gtrsim 1$, especially if the data are noisy. Since the niobium data only have very limited statistics (≈ 300 kEvents per run) it *was not* possible to fit ξ_0 and hence it was fixed to its literature value $\xi_0 = 39$nm (see Ref.[17]).

The resistivity measurements show that the mean free path $\ell \gg \xi_0$, I chose it to a very large value of $\ell = 1000$nm. As long as it is larger than $\approx \xi_0$ it is as if it is ∞ which justify the choice.

I am using the symbol λ_0 to emphasize that it is a fitting parameter. It's physical interpretation is the following: λ_0^{P} is the value extracted by assuming a two fluid model temperature dependence of $\lambda(T) \propto [1-(T/T_c)^4]^{-1/2}$ in the limit $T \to 0$. λ_0^{BCS} corresponds to the weak coupling BCS $\lambda_{\mathrm{L}} = (\mu_0\, ne^2/m)^{-1/2}$. Both is not correct but since a compleat theory to analyze the data is not readily at hand[9] this was the best I could think off. In the case of lead this will lead to interesting results and details like the strong coupling corrections are going to be discussed there.

Lets look at the $B(z)$ (Fig.16) reconstruction more closely. The first thing one notices is that not all the integral reconstructed curves fall nicely on one single curve. The reason for it is mainly the poor statistics. The lead data with higher statistics are not hampered in this respect. Another important observation is that the mean value reconstruction ($\langle B\rangle_{\mathrm{WKM}}$ vs. $\langle z\rangle_{\mathrm{trim.sp}}$) and the integral reconstruction fit very well. This fits the estimate from Sec.2 very nicely if one keeps in mind that we observe a little more than the first decade in B. Last but not least, the $B(z)$ shows a slight curvature as it should be.

[9] strong coupling corrections, details of the electron–phonon coupling, possible reduction of the gap at the surface, ..., see Ref.[18]

8 Lead

8.1 Characterization of the films

The magnetization and resistivity measurements were carried out by Rustem on co–sputtered films.

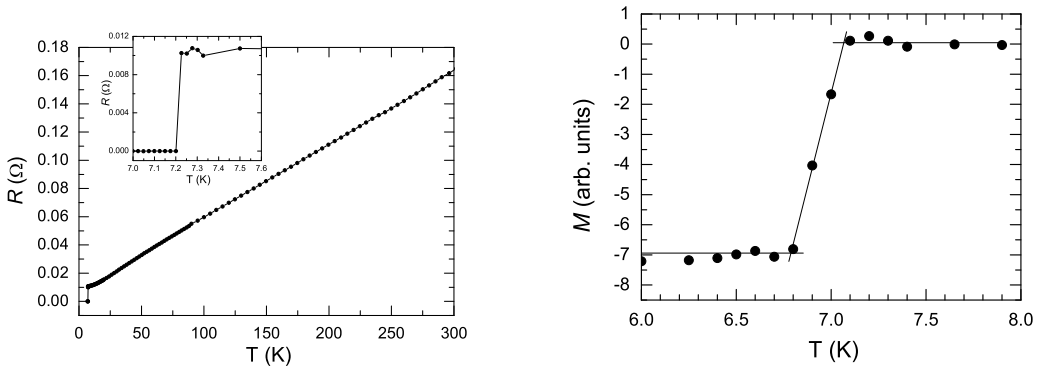

Figure 17: Left graph: Resistance of a part of the 2001 lead film with a $T_c = 7.21(1)$ K. Right graph: Magnetization measurement (2001 Pb film) showing the onset of the Meissner effect at $T_c = 7.1(1)$K.

The oxide layer on top of the film and its thickness were determined by RBS. The results are collected in Table 3. The 2001 oxide layer thickness is definitely an upper limit since it was measured only 3 to 4 month after beam time. I used an operational value of 16nm.

sample	PbO layer (nm)	Pb film (nm)
2001	23(2)	430(20)
2002	5.8(3)	1055(50)

Table 3: RBS values of the lead films. The 2001 film was only measured 3 to 4 month after beam time and therefore the oxide layer thickness is an upper limit.

The mean free path ℓ was estimated by Elvezio Morenzoni (see [11] and Appendix B). The estimated value range from

$$\ell^{\mathrm{Pb}}(T = T_c) \approx 40 \ldots 180 \text{ (nm)}$$

The lower bound of $\ell^{\mathrm{Pb}}(T = T_c)$ is uncomfortably small compared to ξ_0. However, since we do observe the clear deviations from the exponential behavior, ℓ must be larger than ξ_0.

8.2 Pb — Mean Value Reconstruction

The mean value reconstruction was carried out in the same spirt as for niobium, hence details should be checked there (see Sec.7). Some typical stopping profiles are shown in Fig.18, further shows Fig.19 the mean values and backscattering probabilities versus the implantation energy.

There is one aspect which I haven't discussed in the niobium section and this is the meaning of the depolarization rate σ_{Pb} (see Eq.(20)) from the WKM fit. The fitting results are shown in Fig.20. The form of $\sigma_{\mathrm{Pb}}(E_{\mathrm{impl}})$ is always similar. It has a maximum at some intermediate implantation energy and falls off to lower– and higher energies, respectively. Furthermore σ_{Pb} decreases for increasing temperature. All this can be easily understood in a simple static picture. Lets first discuss the form of $\sigma_{\mathrm{Pb}}(E_{\mathrm{impl}})$: At small implantation energies the stopping distribution of the muons is rather narrow and therefore the muons only sample a rather small field range of the magnetic penetration profile, which results in a "small" depolarization rate.

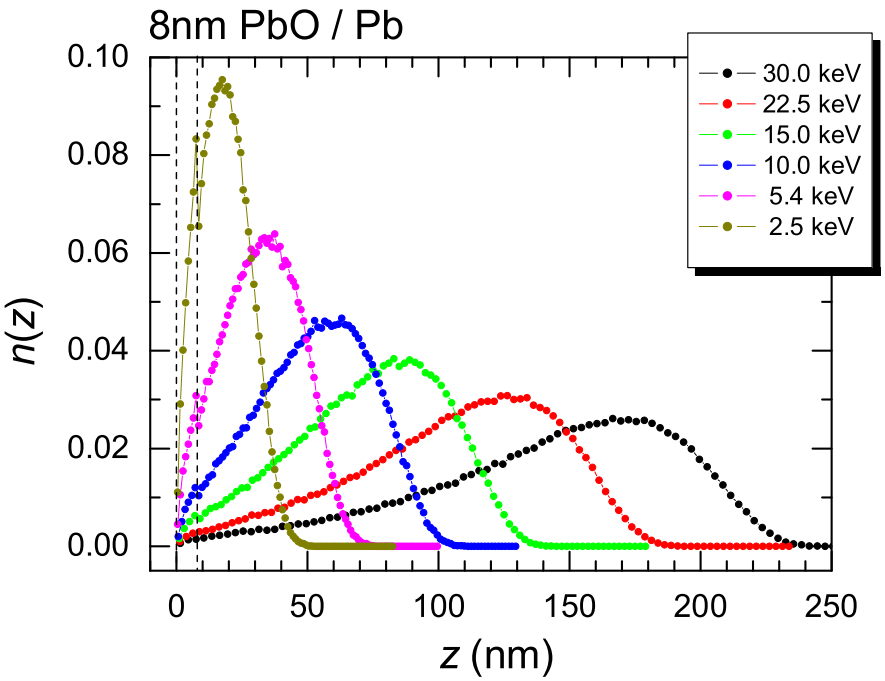

Figure 18: Myon stopping distribution in Lead calculated by `trim.sp`. On top a 8nm PbO film was introduced in the calculation.

At high implantation energies on the other hand, the muon stopping distribution is smeared out considerably but still having a maximum deeper in the sample where the magnetic fields are rather "smallish", hence also the depolarization rate. At intermediate energies there will be a maximum field range sampled by the muons and therefore the maximum in σ_{Pb} results. This can actually modelled in a rather straight forward manner, which was done by Hubertus Luetkens. His result is shown in Fig.21. Hubertus needed to add an offset $\sigma_{\mathrm{offset}} = -0.29(\mu\mathrm{s})^{-1}$. The origin of this offset can have different reasons, e.g. it could be that in the WKM fit the asymmetry (which was fixed, see Sec.7) was chosen systematically too small. Another possibility to explain this discrepancy is that WKM assumes a gaussian model for $p(B)$ whereas the simulation does not assume anything and estimates the real width/σ_{Pb} which might by systematically a little higher. Still, I would like to stress that this rather good agreement shows that the whole analysis is self–consistent and settle.

The temperature dependence of $\sigma_{\mathrm{Pb}}(E_{\mathrm{impl}})$ is also understandable. The decrease of σ_{Pb} for increasing temperature stems from the fact that the penetration depth increases and therefore the magnetic field distribution on the muon stopping length is getting shallower.

8.3 Pb — Integral Reconstruction

As already pointed out in Sec.7.3 this method works very good for $\gtrsim 1$ MEvents, as I will present in the next section.

8.4 Pb — Results and Discussion

The technical details of the analysis I already have described in Sec.7.4, hence I will focus mainly on the physics here. To keep the section svelte, most of the $h(z)$ reconstructed signals are transferred to the Appendix C. The main results are compiled in Table 4. Fig.22 shows a typical $h(z)$ reconstruction. It shows the expected negative curvature, which is much more pronounced than in the case of niobium. This is expected, since lead is a real type I superconductor, i.e. $\varkappa = \lambda_{\mathrm{L}}/\xi_0 < 1$. Again the mean value reconstruction and the integral reconstruction do correspond within the errors, though the integral reconstructed signal with enough statistics

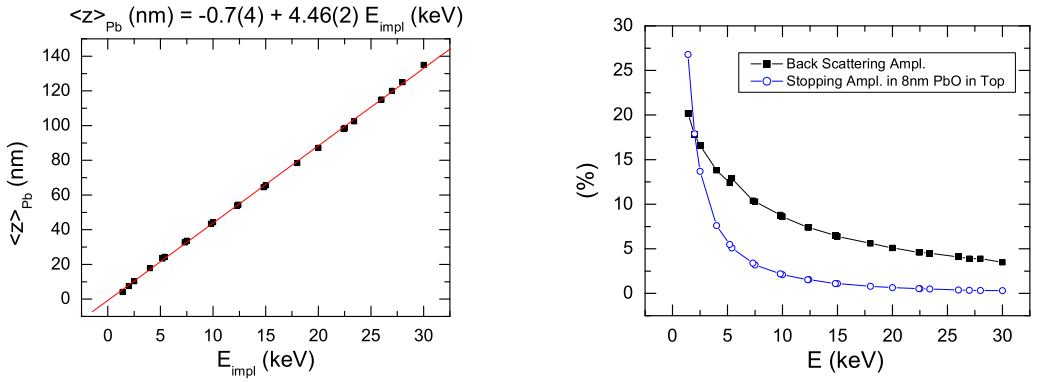

Figure 19: Left graph: E_{impl} vs. $\langle z \rangle$. Right graph: The closed black symbols show the backscattering probability of muons from the surface as function of E_{impl}. The blue open symbols show the stopping probability of the muons in the top layer of PbO.

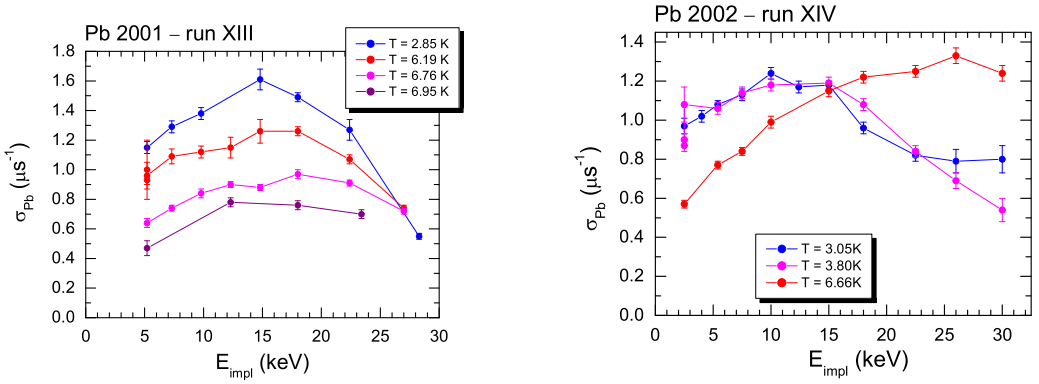

Figure 20: Depolarization rates σ_{Pb} versus E_{impl} for different temperature. The left graph shows the 2001 sample and the right graph the 2002 sample, respectively.

(here ≈ 2 MEvents) gives a much denser curve. The real data almost suggest an even stronger curvature which the models cannot reproduce; this is something I do not understand. Also the general trend as function of temperature is correct, since the $h(z)$'s for values $T \to T_c$ are starting to loose the curvature more and more (see Appendix C).

One thing which seems to be strange is that $\lambda_0^{\mathrm{P,BCS}}$ is temperature dependent (see Tab.4 and Fig.23). This is, however, not surprising. If one recalls the results from the Secs.6.2 & 6.5 it is obvious that neither the twofluid approximation temperature dependence ($\lambda(T) \propto [1-(T/T_c)^4]^{-1/2}$) which went into the estimate of λ_0^{P} nor the BCS one (Eq. (16)) for λ_0^{BCS} will be correct and hence the $\lambda_0^{\mathrm{P,BCS}}$'s will deviate from being constant. The deviation tells us how wrong the assumed temperature dependence actually is. Fig.23 tells us that $\lambda(T) \propto [1-(T/T_c)^4]^{-1/2}$ is a rather good approximation. Since the penetration depth is almost temperature independent for $T \lesssim 0.4T_c$, the low temperature values are the "correct" ones, meaning they do coincide with the simple model parameters.

Now I will come to the discussion of the strong coupling corrections. As pointed out in Sec.6.4 and at the end of Sec.6.5 the strong coupling corrections are *not* changing the structure of the kernel and hence the form of $h(z)$. Therefore it was possible to fit the parameters by using the weak coupling limit and look for the corrections = renormalization afterwards. The relation between the London penetration depth λ_{L} and $\lambda_0^{\mathrm{P,BCS}}$ is according to Sec.6.4

$$\lambda_{\mathrm{L}} \approx \lambda_0^{\mathrm{P,BCS}}/\sqrt{Z}$$

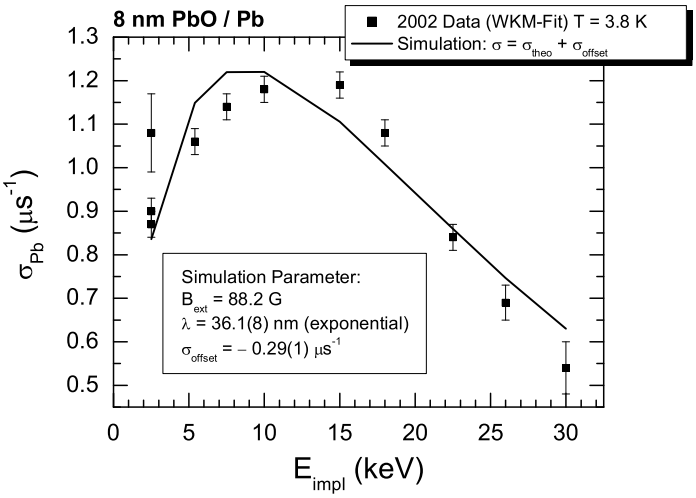

Figure 21: Depolarization rates $\sigma_{\rm Pb}$ versus $E_{\rm impl}$ reconstruction assuming only a static field distribution.

T (K)	$h_{\rm ext}^{T>T_c}$ (G)	$h_{\rm ext}^{\rm P}$ (G)	$\lambda_0^{\rm P}$ (nm)	$h_{\rm ext}^{\rm BCS}$ (G)	$\lambda_0^{\rm BCS}$ (nm)
2001 — run XIII, $\xi_0 = 90$ nm fixed.					
2.85	91.5(5)	87(5)	61(3)	88(4)	58(3)
6.19	91.5(5)	88(5)	61(5)	88(5)	46(4)
6.76	91.5(5)	90(3)	58(3)	91(2)	41(2)
6.95	91.5(5)	91(3)	39(5)	92(3)	32(5)
2002 — run XIV, $\xi_0 = 90(5)$ nm					
3.05	88.2(6)	86(5)	56(1)	86(5)	54(1)
3.8	88.2(6)	88(3)	60(2)	88(3)	55(2)
6.66	88.2(6)	90(2)	59(1)	92(2)	43(1)
3.05	198.6(4)	203(3)	57(3)	204(5)	54(3)

Table 4: Results of the Pb analysis. The mean free path was fixed to $\ell = 100$ nm. This leads to a $\varkappa_{\rm eff} = \lambda_0/\xi_0 = 0.62(4)$. For further details see the text.

where $Z = 1 + \lambda_{\rm e-p}$ [9], with the electron–phonon mass renormalization constant $\lambda_{\rm e-p} \simeq 1.55$ in the case of Pb. Using this formula results in a $\lambda_{\rm L}$

$$\lambda_{\rm L}^{\rm Pb} = 35(2)\ ({\rm nm})$$

The bare coherence length $\xi_0^{\rm bare} = \hbar v_{\rm F}/(2\Delta(0))$ is related to ξ_0 by

$$\xi_0^{\rm bare} \approx \xi_0 \cdot Z$$

which gives

$$\xi_0^{\rm bare}\big|_{\rm Pb} = 230(13)\ ({\rm nm})$$

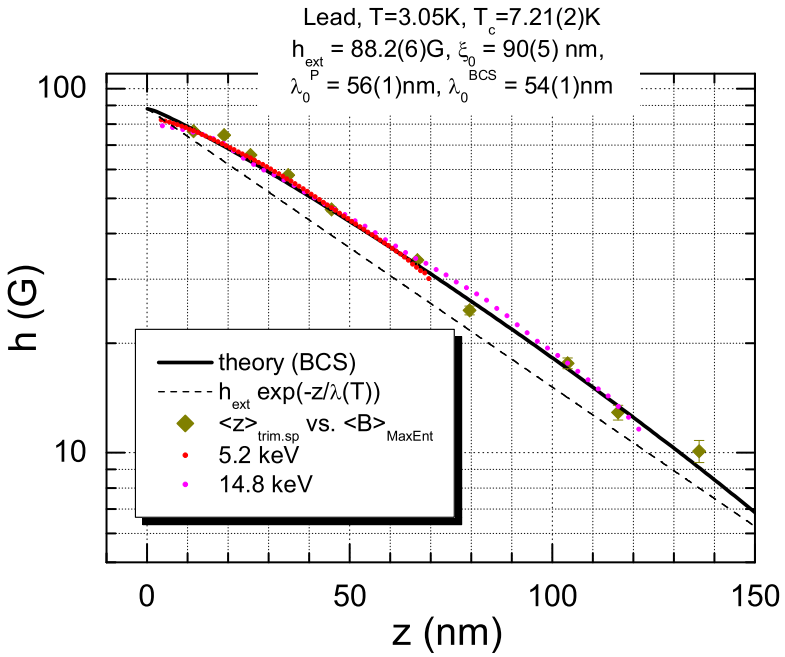

Figure 22: $h(z)$ reconstruction for the 2002 sample — run XIV, $T = 3.05$ K. The dashed line shows an exponential decay with the same λ as the theoretical Pippard and BCS model $h(z)$.

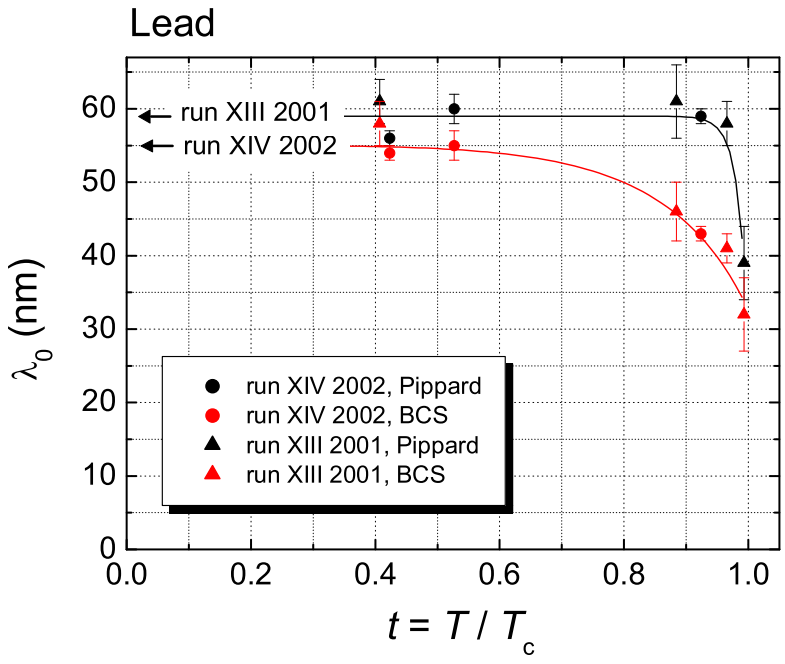

Figure 23: λ_0^α versus T/T_c (α = P, BCS). The curves are guides to the eyes. The red curve is linked to the 2002 sample BCS values, whereas the black curve is linked to the 2001 sample Pippard values.

9 $YBa_2Cu_3O_{7-\delta}$ — A Cross Check

In order to cross check the whole procedure of reconstructing $h(z)$, fitting, etc. I reanalyzed our old $YBa_2Cu_3O_{7-\delta}$ (YBCO) data in the very same manner than the Nb and Pb data (1998 — run XI, 1835 to 1844). Since YBCO is a strong type II superconductor, a perfect exponential $h(z)$ should result[10] (see also Ref.[1]).

The $T = 20$ K results are presented in Fig.24 and indeed show only an exponential decay without any sign of a curvature. Unfortunately we cannot observe a whole decade as for Nb and Pb since the penetration length $\approx 3 \ldots 4$ times larger.

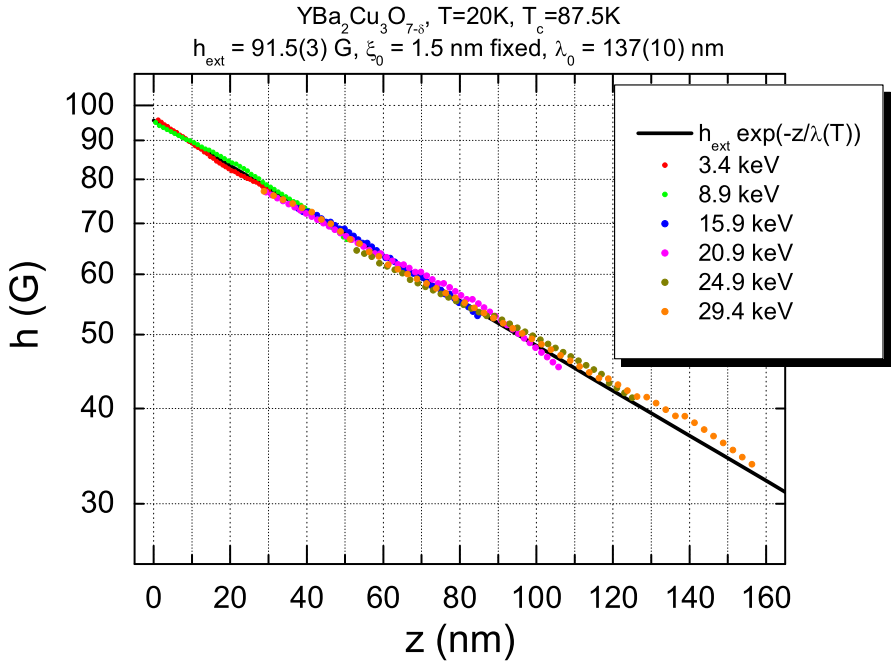

Figure 24: $h(z)$ reconstruction of $YBa_2Cu_3O_{7-\delta}$ for $T = 20$ K.

10 Summary

We measured a Niobium thin film (4.2(1.0)nm NbO / 310(15)nm) with a critical temperature of $T_c = 9.24(6)$K (resistivity) and $T_c = 9.2(1)$K (SQUID), respectively. The mean free path is $\ell =$??nm which shows that we are in the clean limit. We observe small but clear deviation from the exponential magnetic screening in the Meissner–Ochsenfeld effect which are a clear sign of nonlocal effects. The measured penetration depth is $\lambda_0^{\mathrm{Nb}} = 27(2)$nm. The coherence length ξ_0 needed to be fixed (not good enough statistics) to the literature value of $\xi_0^{\mathrm{Nb}} = 39$nm, hence yielding a $\varkappa_{\mathrm{eff}}^{\mathrm{Nb}} = \lambda_0^{\mathrm{Nb}}/\xi_0^{\mathrm{Nb}} = 0.69(5)$.

We also measured two thin films of Lead (2001 sample — run XIII, 16(2)nm PbO / 430(20)nm Pb and 2002 sample — run XIV ??(?)nm PbO / ??(?)nm Pb) with a $T_c = 7.21(1)$K (resistivity) and $T_c = 7.1(1)$K (SQUID), respectively. The mean free path $\ell \gtrsim 100$nm was estimated which shows that this films are in the clean limit. We observed *clear* deviation from the exponential magnetic screening in the Meissner–Ochsenfeld effect which are a clear sign of nonlocal effects. Since we have some high statistic runs (2 MEvents), it was possible not only to determine λ_0^{Pb} but also ξ_0^{Pb}, with the results (average of the two sample): $\lambda_0^{\mathrm{Pb}} = 55(1)$nm and $\xi_0^{\mathrm{Pb}} = 90(5)$nm. Due to strong coupling corrections the London penetration depth λ_{L} is different than λ_0^{Pb}. They are related by $\lambda_{\mathrm{L}} \approx \lambda_0^{\mathrm{Pb}}/\sqrt{Z}$ with $Z = 2.55$ for Pb, and hence

[10] assuming the film is thick enough so that the two sides are *not* interfere with each other.

$\lambda_{\rm L} \simeq 34(1)$nm. We further could show that the temperature dependence of $\lambda_0^{\rm Pb}(T)$ is close to the one in the two fluid approximation $[1-(T/T_c)^4]^{-1/2}$.

A cross check with $YBa_2Cu_3O_{7-\delta}$, a clear type II superconductor, was carried out. Here the magnetic field penetration was perfect exponentially, as expected, proving that our method to analyze the data is correct.

A Strong Coupling Kernel $\mathbf{K(q, \omega \to 0)}$.

Since we are interested in $h(z)$, an important question is how the kernel $K(q, \omega \to 0)$ is going to change. According to Ref. [7], the kernel has the form

$$\begin{aligned} K(q,\omega\to 0) &= \frac{6\pi}{\Lambda}\mathrm{Re}\left\{\sum_n \frac{2\pi}{\beta}\,\frac{\Delta_n^2}{Z_n(\omega_n^2+\Delta_n^2)(3/2)}\,F_0(S_n)\right\} && (21)\\ S_n &= \frac{qv_\mathrm{F}}{2Z_n\sqrt{\omega_n^2+\Delta_n^2}} && (22)\\ F_0(x) &= \frac{1}{x^3}[(1+x^2)\arctan(x)-x]\\ \omega_n &= \pi k_\mathrm{B}T(2n+1)\\ Z_n &\simeq 1+\lambda_{\mathrm{e-p}} \end{aligned}$$

where I used Nam's notation. This expression was derived in the Matsubara formalism (see Refs. [3], [19]). If one want to compare it with Halbritter's expressions a little bit of algebra leads to

$$\begin{aligned} K(q,\omega\to 0) &= \frac{4\pi}{\Lambda}\mathrm{Re}\left\{\frac{\Lambda}{\Lambda_n}\,\frac{3}{2}\,F_0(q\xi_n)\right\} && (23)\\ \frac{1}{\Lambda_n} &= \frac{2a_n}{\Lambda[1+(2n+1)^2a_n^2]^{3/2}}\cdot\frac{1}{Z_n} && (24)\\ \xi_n &= \frac{\hbar v_\mathrm{F}}{2\Delta_n\sqrt{1+(2n+1)^2a_n^2}}\cdot\frac{1}{Z_n}. \end{aligned}$$

If one assumes $\Delta_n = \Delta(T)$, one sees that kernel has the very same structure, except that with the renormalization

$$\begin{aligned} \lambda_\mathrm{L} &\to \lambda_\mathrm{L}\sqrt{Z}\\ F_0(q\xi) &\to F_0(q\xi/Z) \end{aligned}$$

B Mean Free Path Estimates

Since it is important to have a realistic estimate of the mean free path of the electrons ℓ different methods are compiled here, though no derivations are given.

B.1 Mean Free Path from Resistivity

In Ref.[20] it shown that the following equation holds

$$\rho \cdot \ell \cdot N^{2/3} = \left(\frac{3}{8\pi}\right)^{1/3} \frac{h}{e^2} = 1.27 \cdot 10^4 \ \Omega, \tag{25}$$

where ρ is the resistivity, ℓ the electron mean free path and N the electron density. This equation is derived from a free electron approximation which is by far to crude for Pb and Nb.

Measured values for $\rho \cdot \ell =: C$ [11] can be used to estimate ℓ from direct resistivity measurements carried out by Rustem (see Secs. 8 and 7).

Example Pb: $C^{\mathrm{Pb}} \approx 492 \ \mu\Omega \cdot \mathrm{cm} \cdot \text{Å}$ [11] and $\rho(T = T_c + \epsilon) \approx 1.3 \ \mu\Omega \cdot \mathrm{cm}$ (from Rustems measurements) $\Rightarrow$

$$\ell^{\mathrm{Pb}}(T = T_c + \epsilon) \approx 38 \text{ nm}$$

B.2 Mean Free Path from Fermi-velocity

The Heisenberg uncertainty principle can also be used to estimate the electron mean free path ℓ. Assuming that the electrons are in thermal equilibrium with the lattice the following estimate should hold

$$\frac{\hbar}{\tau} \simeq 2\pi k_{\mathrm{B}} T \cdot \lambda_{\mathrm{e-p}}. \tag{26}$$

Together with $\tau \simeq \ell / \langle v_{\mathrm{F}} \rangle$, one gets

$$\ell \simeq \frac{\hbar \langle v_{\mathrm{F}} \rangle}{2\pi k_{\mathrm{B}} T \cdot \lambda_{\mathrm{e-p}}} \tag{27}$$

For example this will lead, in the case of Pb, with $\langle v_{\mathrm{F}} \rangle^{\mathrm{Pb}} \approx 1.8 \cdot 10^6$ m/s [21], and $\lambda_{\mathrm{e-p}}^{\mathrm{Pb}} \simeq 1.55$ [9], to

$$\ell^{\mathrm{Pb}}(T = T_c + \epsilon) \approx 180 \text{ nm} \tag{28}$$

C Pb — all the $h(z)$ reconstructed signals

Here all the $h(z)$ reconstructed signals are given. For a detailed discussion the reader is refered to Sec.8.4.

C.1 Pb — 2001 sample, run XIII

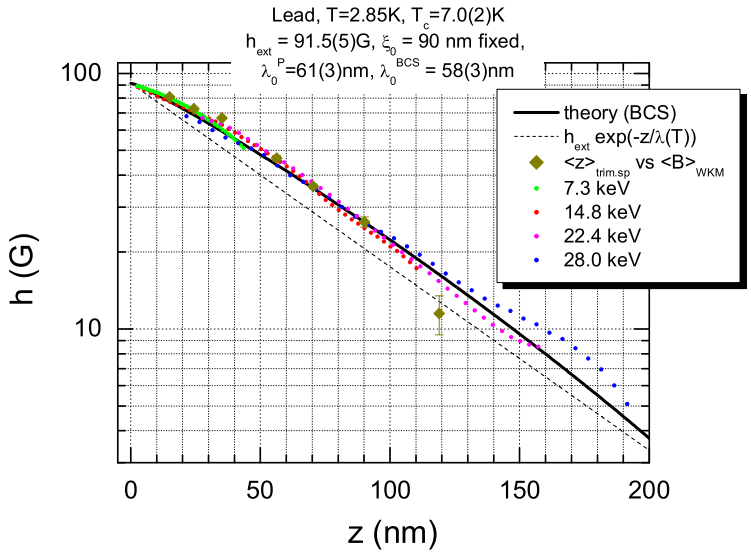

Figure 25: Sample 2001 — run XIII, $T = 2.85$ K.

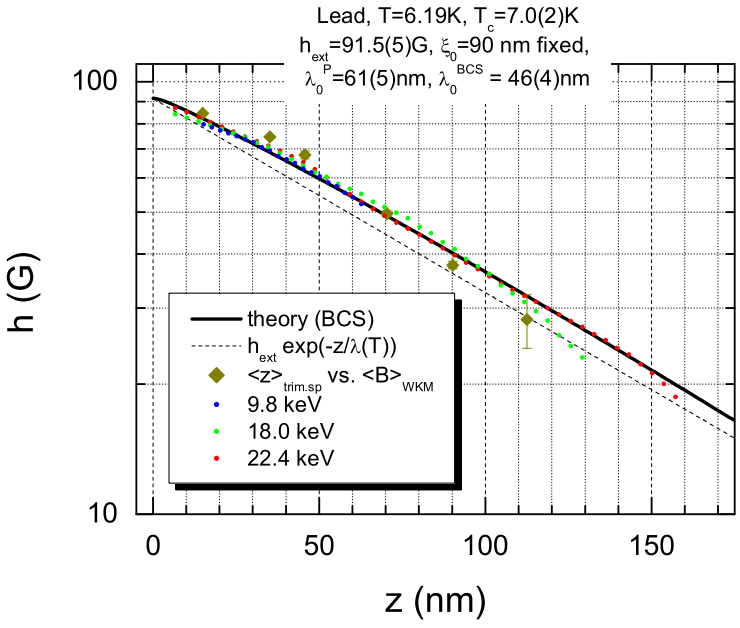

Figure 26: Sample 2001 — run XIII, $T = 6.19$ K.

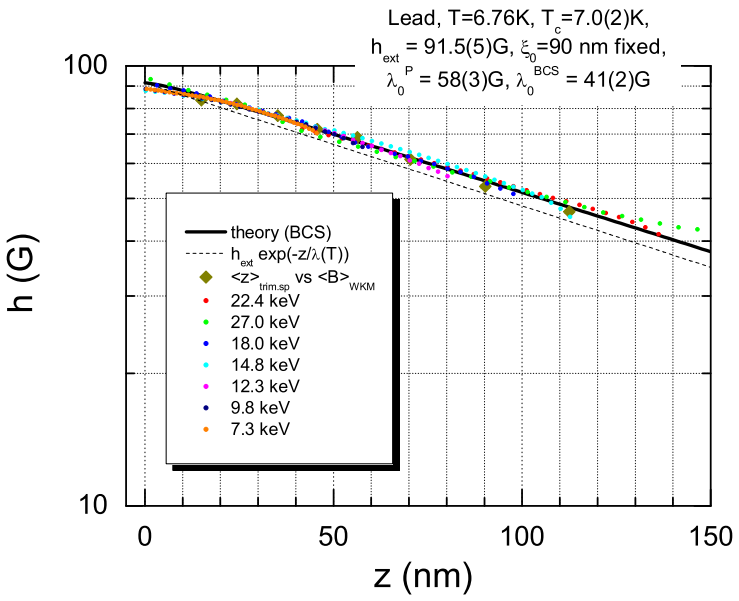

Figure 27: Sample 2001 — run XIII, $T = 6.76$ K.

C.2 Pb — 2002 sample, run XIV

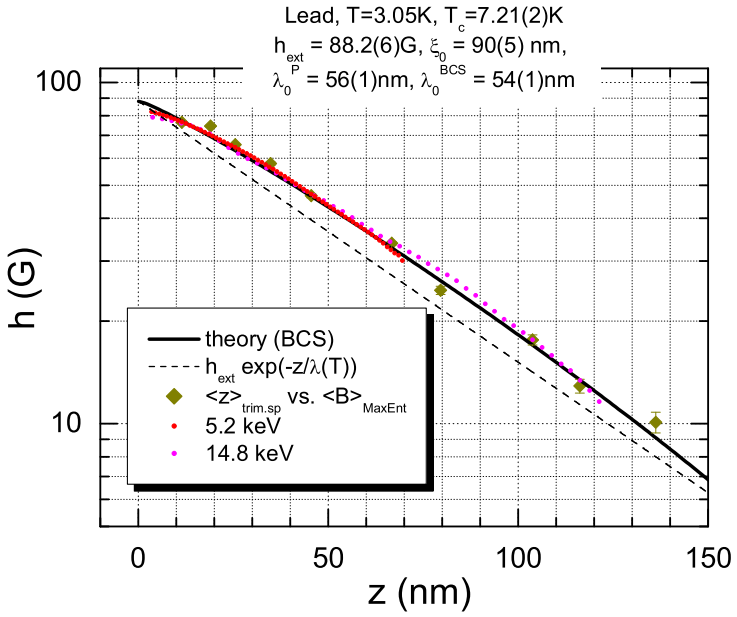

Figure 28: Sample 2002 — run XIV, $T = 3.05$ K.

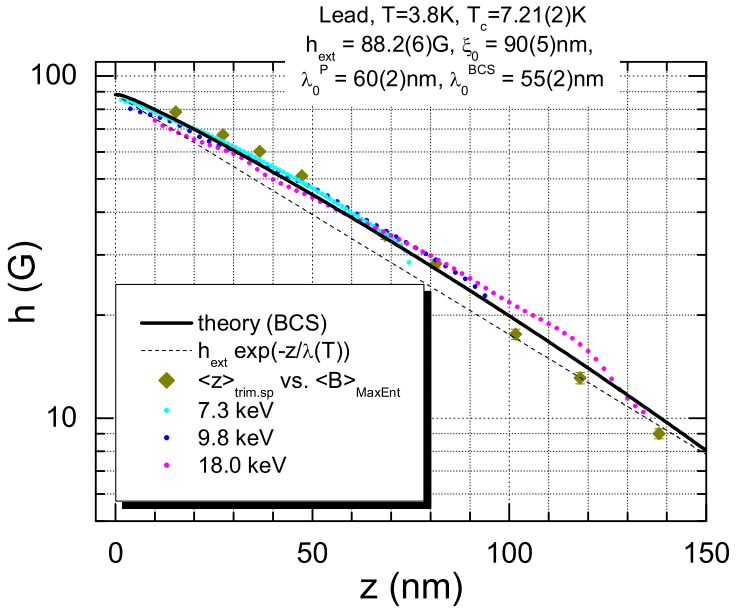

Figure 29: Sample 2002 — run XIV, $T = 3.80$ K.

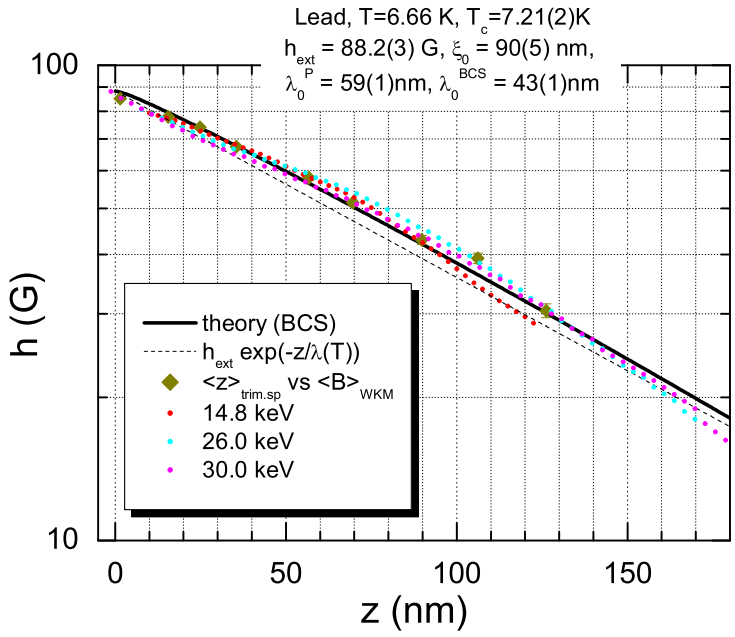

Figure 30: Sample 2002 — run XIV, $T = 6.66$ K.

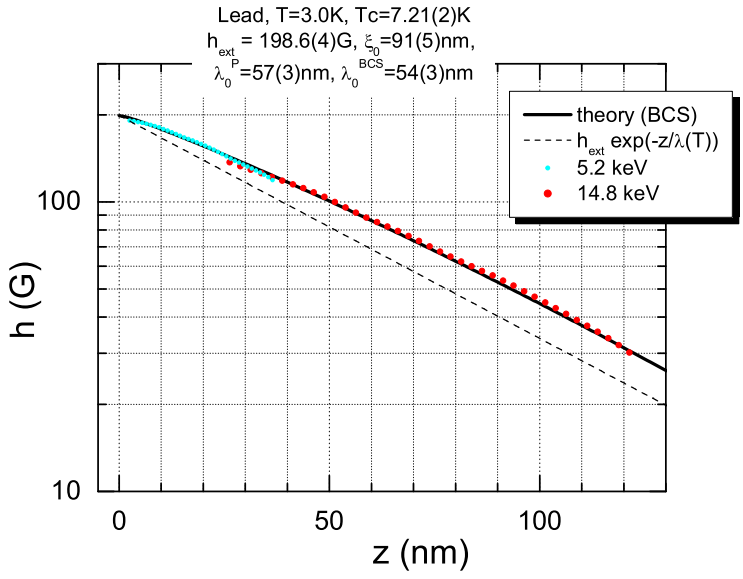

Figure 31: Sample 2002 — run XIV, $T = 3.00$ K, $h_{\text{ext}} = 198.6(4)$ G.

D matlab — integral reconstruction routines

The integral reconstruction used to determine $B(z)$ was carried out in matlab since it is *very* convenient for this kind of tasks. The necessary routines are going to be listed here. For each single run an integral reconstruction file exists, however I only give a single example here.

D.1 matlab — general routines used for the integral reconstruction

```
% reads a MAXENT output file
% SYNTAX: [B,pB] = read_maxent(name);
%         'name' is the *.dat file from the maxent output.
function [B,pB] = read_maxent(name)
h=importdata(name);
B = h.data(:,1)*1e4; % fields in gauss
pB= h.data(:,2);
```

```
% read trim.sp data into matlab
% SYNTAX: [z,pz] = read_trimsp(name)
%         'name' is the filename of the trim.sp *.rge file.
function [z,pz] = read_trimsp(name)
h=importdata(name);
z=h.data(:,1);
pz=h.data(:,2);
clear h;
```

```
% b_of_z.m
%
% evaluates B(z) starting from
%
%   p(z) trim.sp
% and
%   P(B) maxent
%
% the assumption is that B(z) is a monotonic function.
% This assumption is NOT always fulfilled!!!!!
%
% SYNTAX: [z,B]=b_of_z(z_in,pz,B_in,pB,tag)
%         (z_in,pz) comes from trim.sp
%         (B_in,pB) comes from maxent
%         tag: 0 means case I,  starting at z=0 ...
%              1 means case II, starting at z=infinity
function [z,B]=b_of_z(z_in,pz,B_in,pB,tag)
% the trim.sp and maxent input has to be properly normalized
% trim.sp
pz=pz/sum(pz); % i.e. \sum pz*dz = 1
% maxent
pB=pB/sum(pB); % i.e. \sum pB*dB = 1

% generate cumulative sums
if (tag==0) % case I
   sum_pz=cumsum(pz);                    % sum_pz = int_0^x pz dz
   sum_pB=ones(length(pB),1)-cumsum(pB); % sum_Bz = int_B^Bext pB dB
else % case II
   sum_pz=cumsum(pz); % sum_pz = int_0^x pz dz
   sum_pB=cumsum(pB); % sum_Bz = int_0^B pB dB
end;

z=z_in;

% get the correct B value for a given z
B=zeros(length(sum_pz),1); % B vector
for i=1:length(sum_pz)
  if (tag==0) % case I
    [a,b]=min(abs(sum_pB-sum_pz(i)));
  else % case II
```

```
    [a,b]=min(abs(sum_pB-sum_pz(length(sum_pz)-i+1)));
  end;
  B(i)=B_in(b);
end;
```

D.2 matlab — integral reconstruction from the data

```
%-----------------------------------------------------------------
%
% Pb run XIV, 234 + 242, 2.7K(D2)
%
% load 5.2 keV run 0234+0242
[B,pB]=read_maxent('./maxent/lead/lem02_234+242_tdcut.dat');
% subtract background
pBc=pB; ss=2135; ee=2646;
pBc(ss:ee)=-abs((pB(ss)-pB(ee))/(B(ss)-B(ee)))*(B(ss:ee)-B(ss))+pB(ss);
% load trimsp 5.2 keV
[z,pz]=read_trimsp('./stoping_profiles/trimsp/pb08e052.rge');
% solve the integral equation
type = 0; [z_052,B_052]=b_of_z(z,pz,B,pB,type); first_good = 9;
last_good = length(z_052)-25;
%
% exponential fit
param=[90, 300]; % [B0, lambda]
z_oxid=50;
[Bfit,param,err,chis]=fit(z_052(first_good:last_good)-z_oxid,B_052(first_good:last_good),'expo',param,z_oxid);
%
% mapping trim.sp -> maxent assuming exp-modell
Bmap =expo(param,z_oxid,z); pBmap=pz./(Bmap/param(2));
%
% trim.sp output
subplot(2,2,2); plot(z,pz,'o'); xlabel('z (A)'); ylabel('n(z)');
title('pb film , T=2.7K(D2), E_{impl}=5.2keV, run0234+242');
%
% maxent output
subplot(2,2,4); plot(B,pB,'o'); hold on; plot(B,pBc,'r+');
n_pBc=sum(pBc)*abs(B(2)-B(1)); dBmap=diff(Bmap);
dBmap(length(Bmap))=dBmap(length(Bmap)-1);
n_pBmap=sum(pBmap.*abs(dBmap));
plot(Bmap,pBmap/n_pBmap*n_pBc,'k'); xlabel('B (G)');
ylabel('p(B)'); title('run 0234+242');
%
% B(z) result
zmean=[183,258,323,416,523,735,864,1066,1230,1430]-z_oxid;
Bmean=[76.4,74.5,65.7,57.9,46.6,33.8,24.6,17.6,12.9,10.1];
subplot(1,2,1);
semilogy(z_052(first_good:last_good)-z_oxid,B_052(first_good:last_good),'ro');
hold on semilogy(z_052(first_good:last_good)-z_oxid,Bfit,'k');
semilogy(zmean, Bmean, 'b*'); xlabel('z (A)'); ylabel('B (G)'); if
(type == 0)
    str = 'type = 0, i.e. starting at z=0';
else
    str = 'type = 1, i.e. starting at z=infinity';
end; title(['run 0234+242 - ', str]);
gtext(['B_{ext}=',num2str(param(1)),'\pm',num2str(abs(err(1,1)-err(1,2))),'(G)']);
gtext(['\lambda_{exp}=',num2str(param(2)),'\pm',num2str(abs(err(2,1)-err(2,2))),'(A)']);
gtext(['z_{oxid}=',num2str(z_oxid),' (A)']);
gtext(date);
%
% write h vs z into a data file
fid=fopen('pb_T2_7K_E052_0234+242.dat','w');

fprintf(fid, '%% pb_T2_7K_E052_0234+242.dat\n');
fprintf(fid, '%% thin film of lead, T=2.7K(D2), E_impl=5.2 keV\n');
fprintf(fid, '%%\n');
fprintf(fid, '%% run XIV 2002 - 0234+242\n');
fprintf(fid, '%% T=3.0K\n');
if (type==0)
    str='0';
else
```

```
    str='infinity';
end;
fprintf(fid, '%% reconstruction type = %d, i.e. starting from z=%s.\n', type, str);
fprintf(fid, '%%\n');
fprintf(fid, '%% Andreas Suter, %s\n', date);
fprintf(fid, '%%\n');
fprintf(fid, '%% z (nm), B (G)\n');

for i=first_good:last_good
  fprintf(fid, '%f, %f\n', (z_052(i)-z_oxid)/10, B_052(i));
end;

fprintf(fid, '%% end of data\n');

fclose(fid);
```

References

[1] T. Jackson *et al.*, Phys. Rev. Lett. **84**, 4958 (2000).

[2] J. Bardeen, L. Cooper, and J. Schrieffer, Phys. Rev. **108**, 1175 (1957).

[3] J. Schrieffer, *Theory of Superconductivity* (Addison Wesley, San Francisco, 1988).

[4] M. Tinkham, *Introduction to Superconductivity* (Krieger, New York, 1980).

[5] A. Pippard, Proc. Roy. Soc. (London) **A216**, 547 (1953).

[6] J. Halbritter, Z. Phys. **243**, 201 (1971).

[7] S. Nam, Phys. Rev. **156**, 470 (1967).

[8] J. Swihart and W. Shaw, Physica **55**, 678 (1971).

[9] J. Carbotte, Rev. Mod. Phys. **62**, 1027 (1990).

[10] B. Mühlschlegel, Z. Phys. **155**, 313 (1959).

[11] E. Morenzoni, Notes and refences therein.

[12] W. Eckstein, *Computer Simulation of Ion-Solid Interactions* (Springer, Berlin, 1991).

[13] E. Morenzoni *et al.*, Nucl. Instrum. Methods **192**, 254 (2002).

[14] J. Halbritter, Appl. Phys. A **43**, 1 (1987).

[15] F. James and M. Goossens, *Minuit*, CERN-CN Division, Geneva, 1992.

[16] N. U. Association, *NAG C Library*, The Numerical Algorithms Group Ltd., Oxford, 1998.

[17] C. Poole, H. Farach, and R. Creswick, *Superconductivity* (Academic Press, San Diego, 1995).

[18] *Superconductivity*, edited by R. Parks (Dekker, New York, 1969).

[19] W. Nolting, *Grundkurs Theoretische Physik — Viel-Teilchen-Theorie* (vieweg, Braunschweig/Wiesbaden, 1990).

[20] H. Kerchner and D. Ginsberg, Phys. Rev. B **10**, 1916 (1974).

[21] N. Ashcroft and N. Mermin, *Solid State Physics* (W.B. Saunders Company, Orlando, Florida, USA, 1976).